Article

Tuning Catalytic Sites on Zr6O8 Metal Organic Framework Nodes via Ligand and Defect Chemistry probed with t-Butyl Alcohol Dehydration to Isobutylene

Dong Yang, Carlo Alberto Gaggioli, Debmalya Ray, Melike Babucci, Laura Gagliardi, and Bruce C. Gates

J. Am. Chem. Soc., **Just Accepted Manuscript** • DOI: 10.1021/jacs.0c03175 • Publication Date (Web): 05 Apr 2020

Tuning Catalytic Sites on Zr_6O_8 Metal Organic Framework Nodes via Ligand and Defect Chemistry probed with *t*-Butyl Alcohol Dehydration to Isobutylene

Dong Yang,[a†] Carlo Alberto Gaggioli,[b†] Debmalya Ray,[b] Melike Babucci,[a] Laura Gagliardi,[b*] and Bruce C. Gates[a*]

a) Department of Chemical Engineering, University of California, Davis, California 95616, United States

b) Department of Chemistry, Chemical Theory Center, and Minnesota Supercomputing Institute, University of Minnesota, Minneapolis, MN 55455, United States

ABSTRACT: Metal organic frameworks (MOFs) have drawn wide attention as candidate catalysts, but some essential questions about their nature and performance have barely been addressed: 1. How do OH groups on MOF nodes act as catalytic sites? 2. What are the relationships between these groups, node defects, and MOF stability, and how do reaction conditions influence them? 3. What are the interplays between catalytic properties and transport limitations? To address these questions, we report an experimental and theoretical investigation of the catalytic dehydration of *t*-butyl alcohol (TBA) used to probe the activities of OH groups of Zr_6O_8 nodes in the MOFs UiO-66 and MOF-808, which have different densities of vacancy sites and different pore sizes. The results show that (1) terminal node OH groups form as formate and/or acetate ligands present initially on the nodes react with TBA to form esters; (2) these OH groups act as catalytic sites for TBA dehydration to isobutylene; and (3) TBA also reacts to break node-linker bonds to form esters and thereby unzip the MOFs. The small pores of UiO-66 limit the access of TBA and the reaction with the formate/acetate ligands bound within the pores, whereas the larger pores of MOF-808 facilitate transport and favor reaction in the MOF interior. However, after removal of the formate and acetate ligands by reaction with alcohols to form esters, interior active sites in UiO-66 become accessible for the reaction of TBA, with the activity depending on the density of defect sites with terminal OH groups. The number of vacancies on the nodes is important in determining a tradeoff between the catalytic activity of a MOF and its resistance to unzipping. Computations at the level of density functional theory show how the terminal OH groups on node vacancies act as Brønsted bases, facilitating TBA dehydration via a carbocation intermediate in an E1 mechanism; the calculations further illuminate the comparable chemistry of the unzipping.

INTRODUCTION

Metal-organic frameworks (MOFs) are an enormous and rapidly expanding class of crystalline, porous materials formed by coordination of organic linkers with inorganic nodes.[1-3] Some MOFs are good candidate catalysts, offering the advantages of high densities of accessible active sites, high degrees of structural tunability, and high thermal stability.[4-8] MOFs that are exemplary in these respects prominently include those with Zr_6O_8 or Hf_6O_8 nodes, which offer catalytic sites and platforms for catalytic sites.[9-11] Because they are metal oxide clusters, these nodes are comparable to catalysts in an extremely common class, metal oxides, but they are distinct because the node surfaces differ from bulk metal oxide surfaces.[4] An advantage of these MOFs over metal oxides is the structural uniformity of the nodes, in contrast to the heterogeneity of the surfaces of amorphous metal oxides; consequently, fundamental investigations of structure-catalytic property relationships of the MOFs offer the prospect of deeper fundamental understanding than investigations of the metal oxides—and the further prospect of insights from MOF chemistry that extend to metal oxides.

The components on node surfaces—besides the linkers—are typically not represented in MOF crystal structures determined by X-ray diffraction crystallography, because they are often present in such low concentrations as to escape detection. Yet these components, or defects where linkers are missing, may be crucial to MOF reactivity and catalysis. Ligands on node vacancies commonly arise (a) from solvents or products of solvent decomposition during MOF synthesis (e.g., formate, formed from dimethylformamide, DMF);[12-13] (b) from modulators added to facilitate MOF synthesis (e.g., acetate, from acetic acid);[14-15] or (c) from post-synthesis treatments, even including washing (e.g., with solvents that leave behind methoxy, ethoxy, hydroxyl, or sulfate ligands).[16-18] In catalysis, these ligands can act as reaction intermediates (e.g., formate or acetate for esterification); be active sites themselves (e.g., providing proton-donor or acceptor sites); or be reaction inhibitors by blocking active sites on the nodes (e.g., benzoate).[4, 13, 19-20] Removal of such ligands may be essential for creation of catalytic activity, for example, by opening Lewis acid sites to catalyze reactions such as dehydration, condensation, and hydrolysis.[11, 13, 20]

In contrast to the aforementioned ligands on MOF nodes, OH groups on the nodes (like those on metal oxide surfaces) are often regarded as native functional groups, arising from water in the synthesis solvents.[14, 21-22] Often detected by infrared (IR)

spectroscopy,[14, 23] these OH groups offer Brønsted acid and base sites that may play roles in catalysis—but, surprisingly, in view of the catalytic importance of such sites on metal oxides—their subtle chemistry remains to be characterized in depth.[4] Our goals were to better understand this node ligand chemistry, especially including the OH group chemistry, and relate it to catalytic properties of the MOFs.

Beyond chemistry, understanding of mass transport is important for understanding catalysis by porous materials such as MOFs, because it may determine the accessibility of catalytic sites within the pores.[4] This topic is also underexplored, in particular as it pertains to catalysis by defects on MOFs, and we also address it here, along with the linked issues of catalyst stability, which have also been largely overlooked.

We chose MOFs incorporating Zr_6O_8 nodes (UiO-66 and MOF-808) because of their well-established chemistry and the opportunities they offer for modifying the node ligands.[12, 14, 16] As a catalytic test reaction, we chose *t*-butyl alcohol (TBA) dehydration, because it has been well investigated with metal oxide and other solid catalysts (such as zeolites and cation exchange resins), often being considered a prototypical Brønsted acid-catalyzed reaction that is straightforward to investigate, in part because it usually gives only a single dehydration product, isobutylene.[24-25] Our experimental results, bolstered by DFT calculations, identify the catalytic sites as node OH groups; elucidate the catalytic reaction mechanism; provide evidence of how the MOF pore size affects the transport of TBA and the accessibility of interior catalytic sites; and show how the catalysts may be deactivated by unzipping.

RESULTS

Ligands Initially Present on Zr_6O_8 MOF nodes.

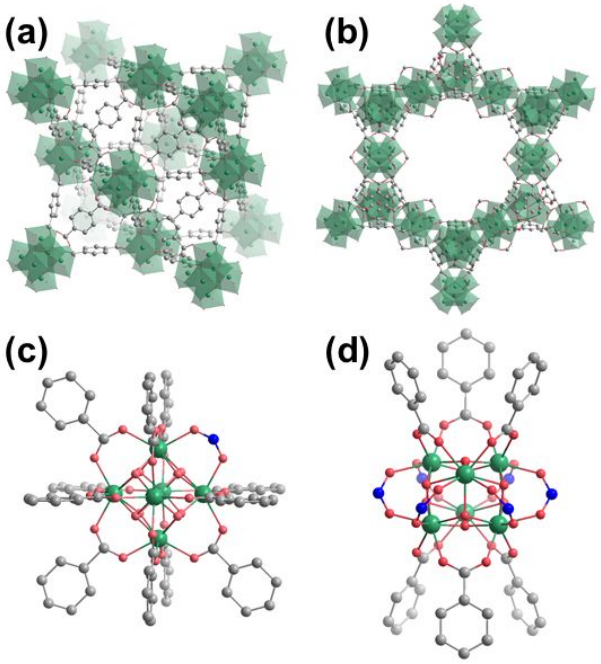

Figure 1. Illustration of crystal structures of (a) UiO-66 and (b) MOF-808, with details showing (c) missing-linker defects of UiO-66 and (d) structural vacancies of MOF-808. Ligands on defects/vacancies are shown in blue.

UiO-66 was synthesized as before[13] with acetic acid as a modulator. Analysis of the MOF by ^{1}H NMR spectroscopy of the solution formed by dissolution of the MOF in NaOH/D_2O (Table 1) showed that a total 1.05 bonding sites per node (excluding linker bonding sites) had been generated during the synthesis—with these sites occupied by acetate ligands (0.80 per node, formed from the acetic acid modulator) and by formate ligands (0.25 per node, formed by decomposition of DMF used in the synthesis).[12-13] IR spectra of the MOF confirm the presence of these ligands, represented by bands at 2953, 2938, and 2923 cm^{-1}, assigned to $\nu_{C\text{-}H}$ of acetate, and at 2747 cm^{-1}, assigned to $\nu_{C\text{-}O} + \delta_{C\text{-}H}$ of formate,[13] matching reported results.[13]

Formic acid was used to modulate the synthesis of MOF-808. Ideally, in the absence of ligands formed from the synthesis mixture, this MOF would have 6 vacancies per node, as indicated by its bulk crystal structure (Figure 1).[26] However, the ^{1}H NMR data characterizing the product formed by dissolution of the MOF in NaOH/D_2O (Table 1) show that each node, on average, was bonded to 4.9 formate ligands, a result bolstered by a strong IR band at 2745 cm^{-1} representing formate on the node vacancies (Figure S1 in the Supporting Information, SI). The IR spectrum of MOF-808 also indicates OH groups (formed by H_2O chemisorption on the nodes), characterized by a band at 3586 cm^{-1} (Figure S1, SI), consistent with the formulation $Zr_6O_5(OH)_3(BTC)_2(HCOO)_5(H_2O)_2$ presented by Yaghi's group,[16] where BTC represents the linker formed from the precursor benzene-1,3,5-tricarboxylic acid.

Table 1. Changes of BET surface areas, numbers of nonlinker ligands per node determined by ^{1}H NMR spectroscopy of dissolved sample, and rates of catalytic TBA dehydration observed for UiO-66 and MOF-808 after various times on stream in the flow reactor at 150 °C and atmospheric pressure.

MOF	Time on stream in the flow reactor used for TBA dehydration, h	BET surface area of MOF (m^2 g^{-1})	Number of formate ligands per node	Number of acetate ligands per node	Total number of nonlinker carboxylate ligands per node	10^3 × rate of TBA conversion, molecules $node^{-1}$ s^{-1}
UiO-66	0	1327	0.25	0.80	1.05	0.02[a]
	6	989	0.18	0.79	0.97	0.17
	13	1047	0.16	0.77	0.93	0.20
	24	988	0.15	0.76	0.91	0.22
MOF-808	0	1591	4.90	-	4.90	2.12[a]
	6	903	2.14	-	2.14	0.47
	13	211	1.76	-	1.76	0.35
	24	104	1.28	-	1.28	0.23

[a]Initial rates were determined by extrapolating differential conversion data to zero time on stream.

TBA Dehydration Catalyzed by UiO-66 and MOF-808.

*Comparison of the MOFs***.** We compared the activities of UiO-66 and MOF-808 for TBA dehydration by using a once-through plug-flow reactor operated at 150 °C and atmospheric pressure, measuring conversions by gas chromatographic (GC) analysis of the product stream. Helium carrier gas flowed through a bubbler in which it was saturated with TBA upstream of the reactor. Catalyst performance data are shown in Figure 2 and Table 1. In contrast to ethanol dehydration (for which diethyl ether was the only dehydration product), the dehydration product of the TBA reaction catalyzed by these MOFs was an olefin, isobutylene, with no detectable ether. MOF-808 was more than 100 times higher in initial activity than UiO-66 under our conditions in the flow reactor (150 °C; 75 mbar of TBA and 924 mbar of helium; total feed TBA flow rate 5.4 mL(NTP)/min; catalyst mass, 25–100 mg).

To understand the contrast between these MOFs, we consider (a) their different stabilities; (b) the differences in the numbers of node sites that were not blocked by formate or acetate (vacancy sites); and (c) the pore sizes, which affect accessibility of the catalytic sites. MOF-808 has, on average, 6 times more vacancy sites per Zr_6O_8 node than UiO-66 (Table 1), and MOF-808 also has a larger pore aperture diameter than UiO-66 (14 vs. 6 Å). We infer that both of these differences are significant in influencing the catalytic properties, as summarized below.

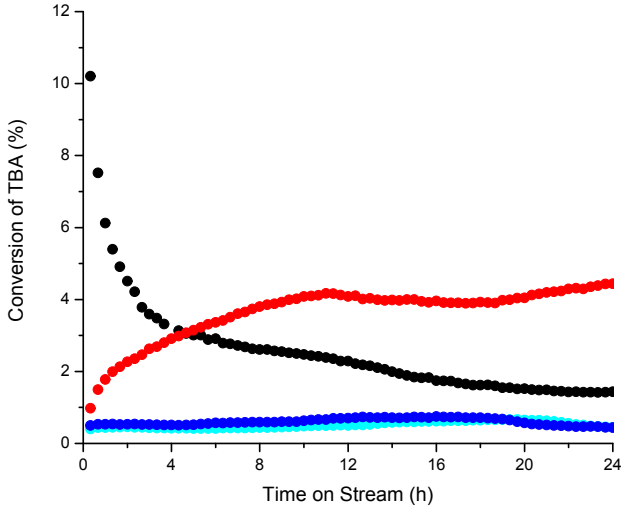

Figure 2. Conversion of TBA in a flow reactor catalyzed by UiO-66 (red), MOF-808 (black), γ-Al_2O_3 (light blue), and ZrO_2 (dark blue). Isobutylene was the only observed product of the catalytic reaction. The results of blank experiments are as follows: with 2 g of inert α-Al_2O_3 but no catalyst in the reactor, the conversion was essentially negligible, only 0.3 ± 0.1%; bare H_2BDC linker was found to be inactive. Reaction conditions: temperature, 150 °C; feed partial pressures, 75 mbar of TBA and 924 mbar of helium; total flow rate 5.4 mL(NTP)/min; catalyst masses: 25 mg of MOF-808 and 100 mg of each of the following: UiO-66, γ-Al_2O_3, and ZrO_2.

Changes in catalysts during operation in a flow reactor. To test for changes in composition and crystallinity of the MOFs as they functioned as catalysts, we determined changes in their structures occurring during the catalytic reaction by making X-ray diffraction (XRD) measurements of the catalysts removed from the reactor after various times on stream, complemented by IR spectra of the catalysts and ^{1}H NMR measurements of the liquid samples formed by dissolution of the catalysts in NaOH in D_2O. The on-line GC data recorded periodically (primarily to determine the product composition and thereby characterize the catalytic activity, Table 1) provide complementary information, showing that ligands initially present on the MOF nodes reacted with the TBA and desorbed, flowing with the reaction products and unconverted reactant to the GC. Thus, the GC data indicate the formation of *t*-butyl acetate and *t*-butyl formate, which formed by the reaction of TBA with the acetate and formate ligands, respectively, that were initially present on the MOF nodes. Figure S7 in the SI shows data demonstrating the formation of these esters from MOF-808 and from UiO-66 during catalysis. The TBA conversion data (measured as the formation of isobutylene) indicate that MOF-808 catalyst was initially about 100 times more active than UiO-66 (Table 1), but it underwent rapid deactivation during operation, with only 11% of the initial activity (measured as rate of reaction determined from differential conversions, Table 1) remaining after 24 h of continuous reaction. XRD data characterizing the catalyst samples that had been used for various times on stream show that the crystallinity of MOF-808 decreased as it functioned as a catalyst, with an almost complete loss of crystallinity after only 13 h onstream; correspondingly, BET surface area data (Table 1) show that MOF-808 had lost most of its porosity after this period. Thus, we infer that the deactivation of MOF-808 resulted from its unzipping, comparable to the deactivation of UiO-66 used for ethanol dehydration catalysis.[13] This unzipping is explained by the breaking of node–linker bonds[13] as TBA reacted with the BTC linkers bonded to the nodes, leading to the formation of esters. Evidence of these esters is provided not only by the aforementioned GC data but also by IR spectra of the used catalysts, with bands at 1710 and 1761 cm^{-1}, attributed respectively to esters and free COOH groups of the unlinked BTC.[27] These IR bands increased in intensity over 24 h of catalyst operation at 150 °C (Figure S2, SI; details of the band assignments are presented in the SI). Further, as a result of reaction with TBA, 74% of the formate ligands initially present on the node vacancies had been removed after 24 h of operation of the catalyst in the flow reactor, as shown by the ^{1}H NMR data (Table 1).

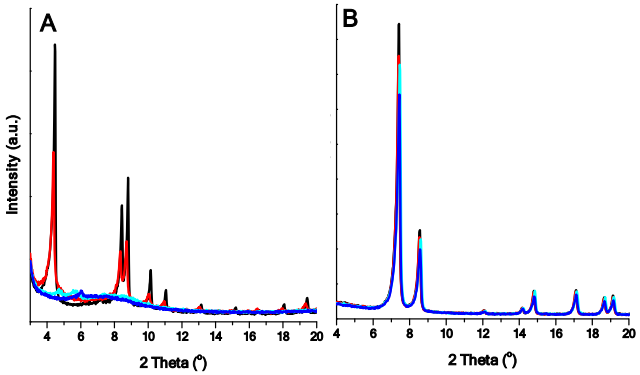

Figure 3. XRD patterns of as-synthesized MOF-808 (A) and UiO-66 AA (B) (black) and the samples after TBA dehydration catalysis

in the flow reactor at 150 °C for the following times on stream (h): 6 (red), 13 (cyan), and 24 (blue).

In contrast to MOF-808, UiO-66 gradually *increased* in activity during catalysis in the flow reactor, so that the activities of the two catalysts became essentially the same after 24 h onstream. The increase was accompanied by the removal of formate and acetate ligands, as shown by the GC analyses indicating the esters that formed by reaction of these ligands with TBA. The data of Figure S7 in the SI show that the amounts of formate and acetate desorbed from UiO-66 were much less than those desorbed from MOF-808, and, consistent with these data, the ^{1}H NMR results confirm that only 13% of these ligands initially present on UiO-66 had been removed after 24 h of continuous catalytic reaction at 150 °C. We infer that the observed activation of the UiO-66 catalyst during operation resulted from the removal of the inhibitor formate and acetate ligands, opening catalytic sites on the nodes. After 24 h of continuous reaction, UiO-66 still had an intact crystal structure with just slightly decreased XRD peak intensities (Figure 3) and a high BET surface area of 988 m^2/g (vs. 1392 m^2/g initially).

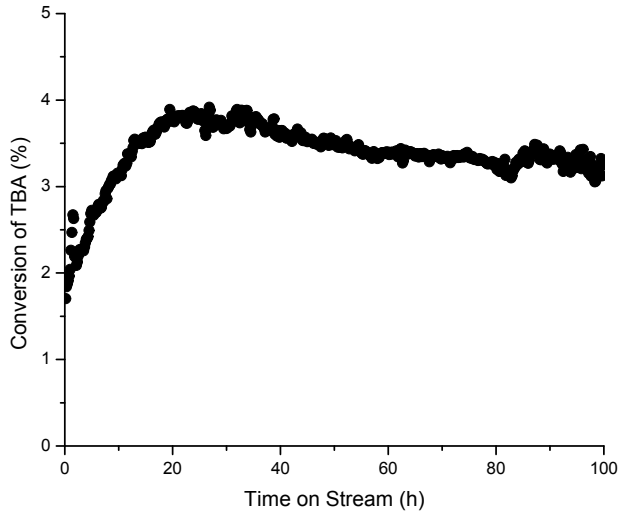

Figure 4. Conversion of TBA to isobutylene catalyzed by UiO-66 in a long-term flow reactor experiment (100 h). Reaction conditions: temperature, 150 °C; feed partial pressures, 75 mbar of TBA and 924 mbar of helium; total flow rate 5.4 mL(NTP)/min; catalyst mass: 100 mg.

To provide further evidence of the stability of UiO-66 under our TBA dehydration conditions, we extended the period of testing from about 24 h (Figure 2) to 100 h. The data from the longer run (Figure 4) show that the activity gradually decreased after a 21-h induction period, indicating that the MOF was being slowly unzipped during catalysis—thus we infer that deactivation was occurring as activation was also occurring initially. The data show that UiO-66 is much more stable than MOF-808, retaining 84% of its highest activity after 100 h onstream. This greater stability of UiO-66 is associated with its far lower density of defect sites per node than MOF-808 (1.05 vs. 6).

On the basis of these data, we infer the collapse of the MOFs led to the formation of aggregated ZrO_2 clusters as well as esters formed by the reaction of linkers with TBA, with all of these being inactive for TBA dehydration at 150 °C.

Role of transport limitations in catalyst pores. In comparing the initial activities of the two MOFs (those with intact structures and the formate and acetate ligands remaining from the syntheses), we need to consider the intrinsic activity, the number of sites not inhibited by formate and acetate, and also the influence of transport effects. Rates of catalytic reactions in porous materials often depend on how fast the reactant molecules are delivered to the catalytic sites: if there is little resistance to transport (e.g., in large pores and/or with small reactant molecules) and the intrinsic activity of the catalyst is low, reactants may reach all the interior sites equally. In contrast, when the transport resistance is large or the intrinsic activity of the catalyst high, the reactants may be largely converted before they reach the interior space of the catalyst—and in the limiting case, all the reaction takes place at the exterior surfaces of the catalyst particles. Because the two MOFs used in this work had the same nodes and similar sites on the node surfaces, but differed markedly from each other in terms of pore geometry and resistance to transport, we infer that transport was important in determining the differences in their catalytic properties. The UiO-66 particles, having pore apertures 6 Å in diameter, nearly matching the critical diameter of TBA (6.1 × 6.7 × 5.7 Å, calculated by DFT), offered more resistance to TBA transport than the MOF-808 (14 Å apertures), so that the initial catalytic activities (Table 1) are consistent with the inference that the TBA reached more interior sites to react on MOF-808 than on UiO-66. But the data also show that most of the defect sites in UiO-66 remained covered with the formate and acetate ligands that were present initially—not being replaced by ligands formed from the TBA and not engaged in the catalysis (Table 1) (that is, there was greater inhibition of node sites on UiO-66 than on MOF-808). Thus, the data are not sufficient for a quantitative resolution of the separate effects of transport and site inhibition in the two MOFs, although it is clear that both are important.

The removal of inhibitors from the UiO-66 sites in TBA dehydration is contrasted with that observed for the same MOF catalyzing the dehydration of ethanol—this smaller alcohol (4.2 × 4.9 × 5.8 Å, calculated by DFT) almost completely removed these ligands from the nodes within 4 h at 150 °C,[13] whereas only 13% of these ligands on the MOF outer surface were removed by TBA after 24 h. However, we stress that the comparison does not afford a quantitative resolution of the reaction/transport tradeoff, and that TBA dehydration is much faster than ethanol dehydration on the MOF nodes, as shown by the lack of measurable catalytic activity of UiO-66 for ethanol dehydration at our reaction temperature of 150 °C.

Tuning the Ligands on Zr_6O_8 MOF nodes of UiO-66.

To provide data characterizing the performance of the undeactivated (not unzipped) catalyst in the absence of the inhibition by formate and acetate on the nodes of UiO-66, we used two methods to remove these ligands from the nodes: (1) treatment of the MOF initially incorporating these ligands with methanol and water to remove them and (2) treatment of the MOF at a high temperature (320 °C) to remove them. We emphasize that UiO-66 maintained its crystallinity under these treatment conditions, but MOF-808 was not stable.

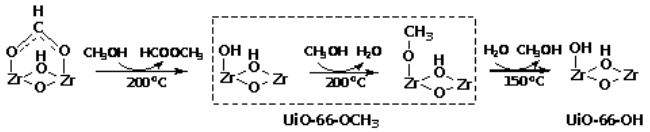

Scheme 1. Topology change resulting from methanol treatment and water treatment inducing reactions on missing linker site of UiO-66 nodes. Reaction between methanol and acetate ligands is suggested to proceed equivalently, with methyl acetate as a product. The sample after methanol treatment at 200 °C, designated as UiO-66-OCH_3, incorporated a mixture of species, as shown in the dashed rectangle. The sample after the subsequent water treatment is denoted as UiO-66-OH.

Our previous results have shown that formate ligands on Zr_6O_8 nodes of UiO-66 react with methanol to form methyl formate and replace the formate with methoxy.[13, 18, 28] To clarify: the change involves two reactions, first, a methanol molecule reacting with a formate ligand to form a methyl formate molecule and a terminal OH group on the node, and, second, a methanol molecule reacting with a terminal OH group to form water and a methoxy ligand (Scheme 1).

To completely remove the formate ligands, we treated UiO-66 (200 mg) with methanol vapor at 200 °C for 48 h, giving a sample designated as UiO-66-OCH_3. After this treatment, IR spectra indicated that formate ligands (with a $\nu_{C-O} + \delta_{C-H}$ band at 2745 cm^{-1}) had been replaced by monodentate methoxy ligands, with ν_{C-H} bands at 2929 and 2826 cm^{-1}, and terminal OH ligands on the nodes, with a ν_{O-H} band at 3778 cm^{-1} (Figure S4, SI). Thus, a mixture of species formed as a result of the methanol treatment. We emphasize that it is difficult to prepare a UiO-66 sample with only methoxy ligands on the nodes under these conditions, because the catalytic methanol dehydration reaction takes place, making dimethyl ether and water—and the water reacts with the methoxy ligands to form methanol and terminal OH ligands. ^{1}H NMR spectroscopy was used to determine the number of methoxy ligands after the methanol treatment. The data (Figure S10, SI) show no evidence of formate or acetate, confirming that they had been completely removed. The data (Figure S10, SI) also show that the UiO-66-OCH_3 sample incorporated 0.45 methoxy ligands per node, which is less than the number per node in the original sample (1.05) and indicates there were terminal OH groups on the nodes, a result that is bolstered by the IR data.

To remove methoxy ligands, we further treated the sample of UiO-66-OCH_3 (200 mg) with flowing water vapor at 150 °C for 10 h, giving a sample designated as UiO-OH. As result of the treatment, all the methoxy ligands were removed, and only terminal OH ligands (characterized by an IR band at 3780 cm^{-1}) remained, as shown by both IR (Figure S5, SI) and ^{1}H NMR data (Figure S11, SI).

Alternatively, formate and acetate ligands on node defect sites of UiO-66 were removed by a high-temperature treatment, which instead led to a dehydrated sample. Following the conditions reported by De Vos et al.,[11] we treated UiO-66 at 320 °C under high vacuum for 12 h. Both IR (Figure S6, SI) and ^{1}H NMR data (Figure S12, SI) show that formate and acetate ligands were completely removed as a result of the treatment. However, the IR spectrum (Figure S6, SI) also shows that terminal OH groups, characterized by a band at 3780 cm^{-1}, and μ_3-OH groups, characterized by a band at 3674 cm^{-1}, were still present, indicating that the sample had not been fully dehydrated. Thus, we infer that a mixture of species (nodes with terminal OH groups and dehydrated nodes) was present in this sample (Scheme 2).

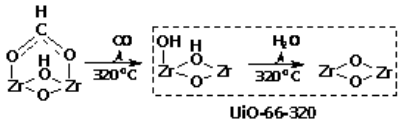

Scheme 2. Topology change of UiO-66 nodes resulting from treatment at 320 °C under high vacuum. Decomposition of acetate ligands is suggested to proceed similarly. The resultant sample is designated as UiO-66-320; the resultant mixture of species in denoted with the dashed rectangle.

Ligand Effect on TBA Dehydration Catalyzed by UiO-66

We tested the catalytic activities of UiO-66-OCH_3, UiO-66-OH, and UiO-66-320 for TBA dehydration to gain more insight into the effects of ligands on node defects and transport limitations.

Similar to the initial UiO-66, UiO-66-OCH_3 increased slightly in activity at the beginning of the flow reactor experiment (Figure 5), accompanied by the desorption of methanol from the catalyst, as detected by GC analysis of the product stream (Figure S8, SI). The data indicate that methoxy ligands on node defects inhibited the reaction, but the inhibition was much less pronounced than that attributed to formate and acetate ligands—because the methoxy ligands are more highly reactive with TBA than the formate and acetate, and, as a result, the induction period (around 3 h) is much shorter than that observed with the as-synthesized MOF (21 h). After the methoxy ligand removal, the sample was gradually deactivated, as a result of the slow unzipping of the MOF. The highest conversion in the reaction with UiO-OCH_3 was 24.7%, corresponding to a reaction rate per node of 1.20×10^{-3} s^{-1} which is 6-fold higher than that observed with the initial UiO-66. We infer that the higher activity of UiO-OCH_3 is a consequence of the greater number of sites opened for catalysis in that sample. On the basis of the activity data, we estimate that 78% (6 × 13%, a ratio of defect sites on the nodes of UiO-66 opened for the catalytic reaction after 24 h) of the defect sites in UiO-66-OCH_3 participated the reaction (assuming the number of defect sites did not change after methanol treatment). However, we emphasize that UiO-66-OCH_3 will have lost some of its defect sites as a result of some unzipping under the methanol treatment conditions of 200 °C for 48 h (catalytic methanol dehydration also took place). Therefore, we infer that the 78% may reflect the number of defects remaining after the methanol treatment, and these were accessible for catalysis.

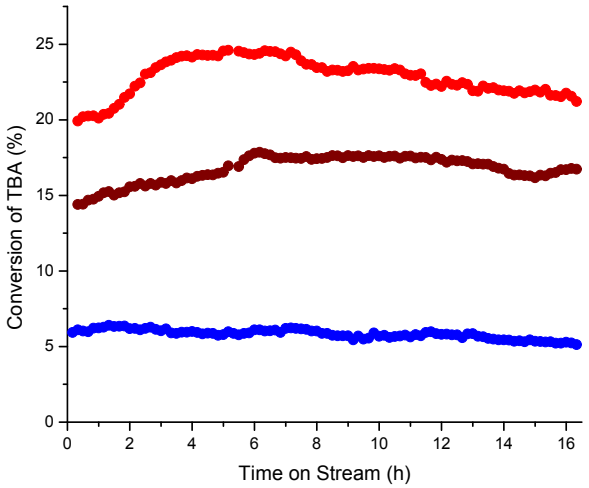

Figure 5. Conversion of TBA to isobutylene catalyzed by UiO-66-OCH_3 (red), UiO-66-OH (brown), and UiO-66-320 (dark blue); isobutylene was the only product of the reaction. Conversion in a blank experiment with 2 g of inert α-Al_2O_3 but no catalyst in the reactor was essentially negligible, only 0.3 ± 0.1%. Reaction conditions: temperature, 150 °C; feed partial pressures, 75 mbar of TBA and 924 mbar of helium; total flow rate 5.4 mL(NTP)/min; catalyst mass, 100 mg.

Because the methoxy ligands had been removed in the treatment with water, the catalysis data characterizing UiO-66-OH were not characterized by a clear induction period (Figure 5). The initial activity of UiO-66-OH was 0.71×10^{-3} s^{-1} (with a conversion of 14.6%), which is 3.5-fold higher than the initial activity of UiO-66 in its as-prepared state but lower than that of UiO-66-OCH_3. We infer that the observed decrease in activity of UiO-66-OCH_3 after water treatment (that is the UiO-66-OH sample) was a consequence of the partial decomposition (unzipping) of the MOF under hydrothermal conditions at 150 °C, as had been shown before.[28]

Because all the organic ligands on the defect sites of UiO-66-320 had been removed, this sample was also characterized by a lack of an induction period in the flow reactor experiments (Figure 5). The initial activity of this sample, 0.31×10^{-3} s^{-1}, is the lowest among the three samples that did not contain formate and/or acetate ligands, and it slowly decreased during catalysis. The low activity is not attributed to the decomposition (unzipping) of the MOF, because the MOF was found by XRD to still be intact after the 320 °C treatment under high vacuum; rather, the deactivation is attributed to dehydration of the MOF, as explained below.

Comparison of MOFs with Metal Oxides as Catalysts.

We also compared the catalytic activities of the MOFs with those of metal oxides, namely, γ-Al_2O_3 and ZrO_2. However, by comparison, each of these oxides had only a low activity at 150 °C (Figure 2). Reported data[29-30] show that γ-Al_2O_3 is active for TBA dehydration to give isobutylene but not ether at temperatures higher than 170 °C. The comparison shows that the catalytic sites on the MOF nodes are significantly different from and intrinsically more active than those on these metal oxides.

Insights into nature of catalytic sites on MOF nodes.

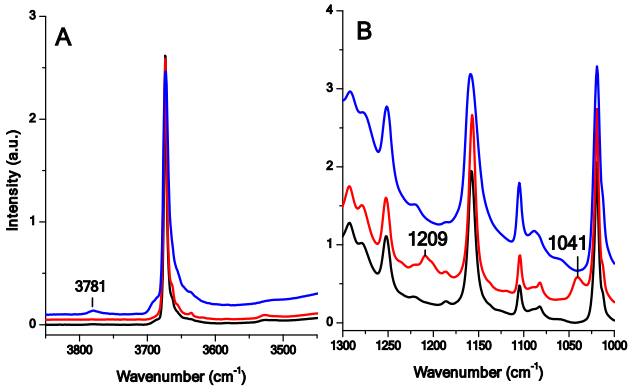

Figure 6. IR spectra charactering as-synthesized UiO-66 (black) and the sample after TBA dehydration catalysis at 150 °C for 6 h (red) followed by treatment under vacuum at 150 °C for 12 h (blue).

Because the as-synthesized UiO-66 underwent gradual activation during catalysis at 150 °C, with the removal of formate and acetate ligands, and because MOF-808 had a much higher initial activity than UiO-66, we inferred, as stated above, that the catalytic sites for TBA dehydration were located at vacancies, with the activity increasing as these opened up during catalysis. To provide more information about the changes, we monitored the MOF structure by IR spectroscopy (Figure 6). After 6 h of catalytic reaction, two new bands had appeared, at 1041 and 1209 cm^{-1}, which nearly match the bands of TBA in the liquid phase, at 1016 and 1200 cm^{-1}.[31] The differences in frequencies of these bands indicate a significant interaction of the alcohol with node vacancies, but the interaction did not lead to the formation of *t*-butoxy ligands (as inferred from the IR data[32]: zirconium *t*-butoxide has IR bands at 1002 and 1186 cm^{-1}).

To further clarify the chemistry, we evacuated the UiO-66 sample after 6 h of catalytic reaction, holding it at 150 °C for 12 h. The resulting IR spectrum shows that bands characteristic of TBA had disappeared, as confirmed by ^{1}H NMR spectra of the sample dissolved in NaOH/D_2O. In contrast, reported results show that ethoxy ligands formed from ethanol on Zr_6O_8 nodes were quite stable under vacuum at 150 °C, and that their formation was accompanied by the appearance of a new band in the IR spectrum at 3781 cm^{-1}, assigned to terminal OH groups on Zr_6O_8 nodes.[13-14] All the data are consistent with the inference that these terminal OH groups were generated as formate and acetate ligands were removed, and when the alcohol was TBA, *t*-butyl formate (and *t*-butyl acetate) desorbed, according to the chemistry shown in Scheme 3.

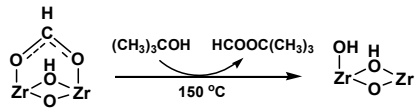

Scheme 3. Topology change of UiO-66 nodes resulting from reaction of TBA with missing linker sites. Reaction between TBA and acetate ligands is suggested to proceed equivalently with $CH_3COOC(CH_3)_3$ as a product.

Consistent with all the data, we further infer that TBA dehydration is catalyzed by these terminal OH groups, with the strongest basis for this inference being DFT calculations, described below. This mechanism is contrasted to the mechanism of ethanol dehydration on the nodes (which proceeds via ethoxy ligands bonded to Lewis acid vacancies of node defects[13]).

This interpretation is bolstered by the catalytic activities of the three samples (UiO-OCH_3, UiO-OH, and UiO-320) without formate and acetate ligands. These samples all had terminal OH groups as initial ligands that were accessible to TBA—and these account for the high initial activities of these samples.

Recall that UiO-OCH_3 incorporated both OH and methoxy ligands and that the latter are highly reactive and readily removed with the formation of terminal OH groups by reaction with water (formed by the dehydration of TBA). Thus, this is the sample that had the highest density of terminal OH groups among all those we investigated.

UiO-66-320 was a highly dehydrated sample, meaning that its defect sites were mostly dehydrated (Lewis acid) sites, as shown in Scheme 2 (the species at the far right). Because the activity of UiO-66-320 was much lower than that of UiO-66-OCH_3, we infer that these Lewis acid sites in the former sample were inactive or barely active for the dehydration of TBA. Reported results[18] show that the rehydration of dehydrated Zr_6O_8 nodes is very slow.

Again, we used in-situ IR spectroscopy, monitoring the changes in UiO-66-OCH_3 and UiO-66-OH during TBA dehydration catalysis. The data show that the IR bands of terminal OH groups at 3780 cm^{-1} and of methoxy ligands at 2826 and 2929 cm^{-1} all disappeared after contact with TBA at 150 °C; correspondingly, IR bands characterizing node vacancy-bonded TBA-derived species appeared at 2975, 1201, and 1037 cm^{-1} (Figure S4-S5, SI). We infer from the aforementioned data, including the catalyst performance data, that methoxy ligands were removed during catalysis and replaced by terminal OH groups. We emphasize that the TBA-derived species observed here were not physisorbed TBA, because these species were not removed by purging with helium at 150 °C and, further, because the intensity of the 2975 cm^{-1} band is correlated with the catalytic activities of UiO-66, UiO-66-OH, and UiO-66-OCH_3. Because TBA did not form *t*-butoxy ligands, we suggest that it likely bonds to the open Zr sites shown in Scheme 3 and interacted with terminal OH groups on neighboring Zr sites, likely forming hydrogen bonds with them.

Because the initial activity of UiO-66 was low (Table 1), we infer that the four μ_3-OH groups that were initially present on each Zr_6O_8 node (each node should nominally be expected to be $[Zr_6(\mu_3\text{-}O)_4(\mu_3\text{-}OH)_4]^{12+}$) lack significant activity for the TBA dehydration reaction. These hydroxyl groups are, we infer, isolated by linkers and lacking neighboring Lewis acid sites, so that they are not effective by themselves for catalyzing the dehydration reaction.

Kinetic isotope effect in MOF-catalyzed TBA dehydration

To provide more insight into the mechanism of the catalytic reaction, we did experiments to determine the kinetic isotopic effect (KIE), using TBA-d_{10} as the reactant and UiO-66-320 as the catalyst operating under conditions of minimal deactivation. The conditions were chosen on the basis of vapor pressure data[33] to give the same partial pressures of TBA and TBA-d_{10} in the comparison experiments. The measured TOF_H/TOF_D value is 2.0 (calculated from the respective differential conversions of 6.3%/3.2%, Figure 5 and Figure S13, SI); below, this value is compared with the value determined by density functional theory.

Characterization of TBA Dehydration Mechanism by Density Functional Theory (DFT).

Formate removal from nodes through esterification with TBA. To gain insight into the mechanisms of the esterification reaction involving TBA and node-bound formate, we conducted a DFT mechanistic investigation, modeling UiO-66 and MOF-808 as described in Figure S15 in the SI.

We started the investigation with UiO-66, and analyzed four pathways for the esterification involving TBA and formate (but calculations were not done for acetate—as we expect that the electronic effects of the acetate group are so similar to those of the formate group that the results presented here can be extended to the esterification involving TBA and acetate). We analyzed four separate pathways, involving one or two TBA molecules in the mechanisms. In the following we show the free energy diagram for the pathway having the lowest activation energy among the four analyzed (path 1, Figure 7).

The reaction starts (Figure 7) with UiO-66 having a formate group bonded to Zr atoms and two TBA molecules at infinite distance. The formate groups are labile ligands, and one Zr bonding site can be opened up for binding with one TBA molecule (highlighted in red, structure **B**). This structure locates at 3.1 kcal/mol. The proton of the alcohol now becomes part of a more strongly acidic group (because TBA is interacting with Zr, a Lewis acid site), and it can protonate the formate to go to structure **C** (through TS BC at 30.1 kcal/mol). Then the OR group (with R being *t*-butyl) can act as a nucleophile and attack the C atoms of the formate to produce structure **D**, with a tetrahedral coordination around the carbon atom of the formate. The **TS CD** is located at 35.7 kcal/mol. We then invoke a second TBA molecule that binds to Zr (highlighted in red in structure **E**), having found that this binding is energetically favorable, lowering the free energy of structure **D** by 5.4 kcal/mol. The next step is the removal of the OH group bonded to carbon by making use of the acidity of the μ_3-OH group, forming water and *t*-butyl formate (structure **F**). The transition state **EF** lies at 40.3 kcal/mol, and it is characterized by the highest activation energy of the whole mechanism—that is, the reaction from **E** to **F** is the rate determining step (RDS). The subsequent removal of *t*-butyl formate and binding of water to Zr lower the free energy, forming structure **G**. Then the protonation of the μ_3-O group (in structure **G**) by the adjacent water molecule occurs through **TS GH**, and structure **H** is formed, in which the TBA and an OH group are bonded to the Zr atoms. The installation of an OH group bonded to Zr is

consistent with the experimental findings, and this is the initial structure for the subsequent TBA dehydration catalysis.

We then questioned whether the steric hindrance of two *t*-butyl groups would preclude the formation of structure **E**. In other words, we wanted to check whether structure **E** could fit into the pore of UiO-66. To achieve this, we recurred to geometry optimization of structure **E** using periodic boundary conditions (PBC, see SI Section S2.2), which takes into account the periodic structure of the MOF and therefore the dimensions of the pores. In Table S1 in the SI, the optimized lattice parameters (lengths, angles, and unit cell volume) for structure **E** and UiO-66 with one missing linker (capped with a water and an OH group) are reported. From the PBC optimization of structure **E** we did not notice a major change in lattice parameters (using UiO-66 with one missing linker as a reference), with a slight contraction of about 0.5 Å (out of 25.5 Å) along the a and c axes and a small change (less than one degree) in angles. The slight contraction of the lattice parameters results in a shrinking of the unit cell volume by only about 2%, which we infer is probably a consequence of dispersion interactions between structure **E** and the linkers. According to these calculations, we can safely conclude that structure **E** is a plausible intermediate for the esterification mechanism and it can well fit into the pore of the UiO-66 MOF.

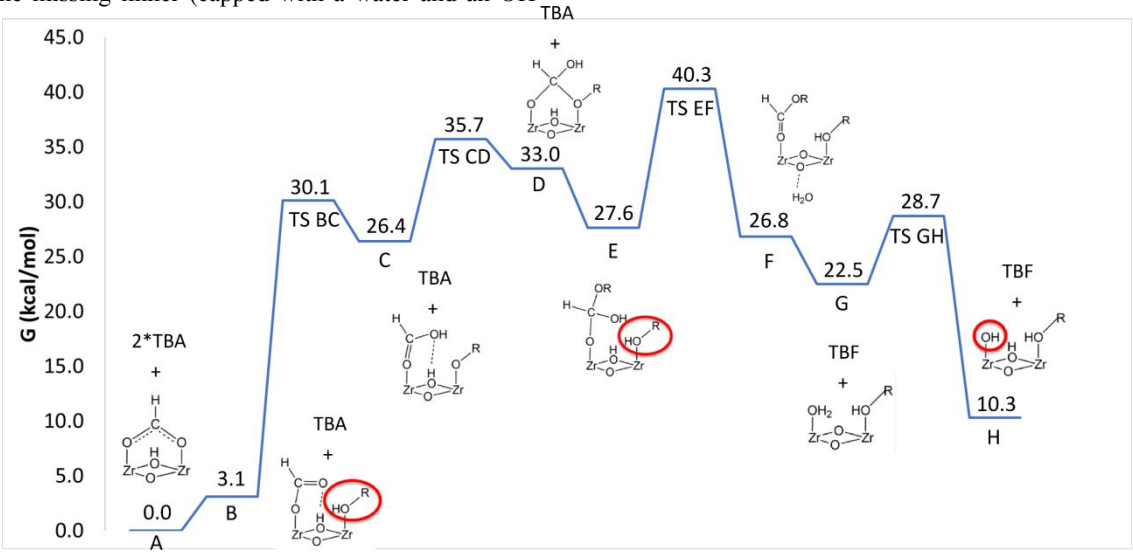

Figure 7: Free energy reaction profile for the esterification reaction between formate and TBA for UiO-66, path 1. The last structure contains a terminal OH group, as inferred from the experimental results. TBA = *t*-butyl alcohol, TBF = *t*-butyl formate, R = *t*-butyl. The alcohol molecules bonded to Zr and the OH group that is formed after esterification are highlighted with red circles.

After examining the mechanism characterized by the lowest activation energy, we briefly discuss the other three pathways, which are characterized by higher activation energies (the free energy diagrams are shown in the SI, Figure S16–S18). In path 2 (Figure S16) the mechanism is the same as the one shown in Figure 7, except that only one TBA molecule is invoked in the reaction. Therefore, structures from **A** to **D** are the same as in Figure 7, but then the protonation of the OH group by the H of the μ_3-OH (**TS DE** in Figure S16) now lies at 45.2 kcal/mol, about 5 kcal/mol higher than the RDS activation energy shown in Figure 7.

The other two analyzed pathways do not involve the binding of TBA to the Zr atoms. Path 3 is shown in Figure S17 in the SI, with the RDS transition state in which the oxygen atom of the alcohol attacks the carbon of the formate and the hydrogen of the alcohol binds to one of the oxygen atoms of the formate, in a concerted way (**TS BC** in figure S17). This transition state locates at 50.9, about 10 kcal/mol higher than the RDS activation energy for the path in Figure 7. The pathway then proceeds with the formation of a tetrahedral structure around the carbon atom of the formate (structure **C**), in which then the C–OH bond easily breaks to form *t*-butyl formate and an OH group bonded to Zr, going down in free energy (structure **D**). The last analyzed path is shown in Figure S18 in the SI and proceeds through a RDS transition state similar to the one shown in Figure S18, in which the H of the alcohol now binds to the μ_3-O group (instead of the oxygen of the formate). This transition state locates at a very high energy, namely, 49.1 kcal/mol. We therefore have not continued the computation of this mechanism.

We then computed path 1 for MOF-808, to determine whether there was any significant difference between the two MOFs, and the results are shown in Figure S19. From these results we see that the RDS for MOF-MOF-808 is 39.5 kcal/mol, which is very similar to what we computed for UiO-66.

In summary, DFT shows that removal of the formate groups via esterification with TBA is characterized by lower activation energies if the binding of two TBA molecules to Zr atoms is invoked. Pathways that do not involve this binding (or only one TBA molecule binding to Zr) proceed through higher energy RDSs. The lowest RDS activation energies we could find are 40.4 kcal/mol for UiO-66 and 39.5 kcal/mol for MOF-808, which are quite high, and corroborate the difficulty in removing formate groups through esterification with TBA, as was observed experimentally.

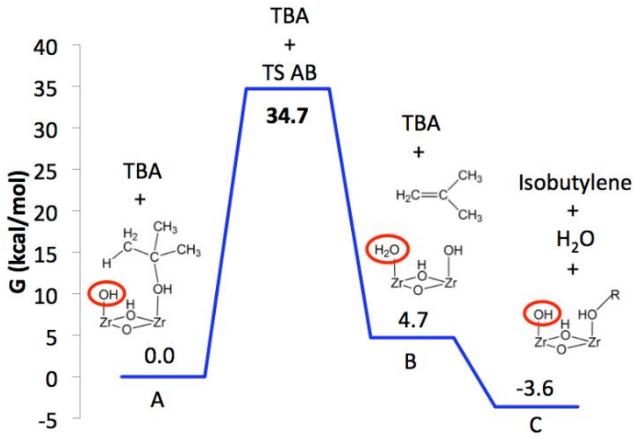

Figure 8: Free energy reaction profile for the TBA dehydration reaction to isobutylene and water for UiO-66. TBA = *t*-butyl alcohol, R = *t*-butyl. The OH group that acts as a Brønsted base and the water formed on the node are highlighted with red circles.

TBA dehydration. To elucidate the TBA dehydration mechanism and the role of the terminal OH group in the catalysis, we carried out a DFT mechanistic investigation. To compare our results with the reported computational investigation of ethanol dehydration on UiO-66, we used the same model and computational details as before.[13] The description of this model and computational details are reported in the SI, Figure S20 and Section S2.4, respectively. The mechanism we found for TBA dehydration reaction for UiO-66 is shown in Figure 8.

The catalysis starts with the OH group and TBA bonded to Zr and an isolated TBA molecule (structure **A**). The reaction then proceeds through the transition state (**TS AB**) located at 34.7 kcal/mol, which produces structure **B** that lies at 4.7 kcal/mol. In the latter, water and an OH group (the leaving group from TBA) are bonded to Zr, and isobutylene is formed, which is still interacting with the node. Finally, to restore the initial structure and close the catalytic cycle, the removal of isobutylene and water and the bonding of a TBA molecule to Zr occur (structure **C**). The overall reaction is exothermic, with structure **C** locating at -3.6 kcal/mol. An important point is that the barrier for this reaction is 4.0 kcal/mol lower than the one reported for ethanol dehydration.[13] This result is in agreement with the higher TOF for the TBA dehydration (see above, experimental results).

In the following, the transition state geometry (**TS AB** in Figure 8) is shown (Figure 9). The analysis of this geometry can provide insights into the mechanism of the TBA dehydration.

In Figure 9 it is noted that the carbon–oxygen bond of the alcohol is highly stretched (2.77 Å), indicating that a tertiary carbocation is formed. The C–H bond that is being broken (blue number) is 1.20 Å, which is not highly stretched compared with another C–H bond of the alcohol that does not participate in the reaction (1.10 Å, red number). The O–H bond (to form water) is not yet fully formed (1.53 Å in Figure 9). According to this geometry, we can conclude that the mechanism of the TBA dehydration is consistent with an E1 elimination. However, the E1 mechanism consists of two different transition states, the first characterizing the formation of the carbocation and the second characterizing the C–H bond activation. In the mechanism we propose in Figure 8, only one transition state has been located (consisting of a concerted breaking of the C–O and C–H bonds of the alcohol) and all attempts to stabilize a carbocation intermediate were not successful (that is, the structure would optimize either to reactant or to product). This result is probably an indication that the reaction takes place with gas-phase reactants, and that no solvent is present to stabilize a positive charge. Nevertheless, the highly stretched C–O bond of the alcohol in the TS indicates that a carbocation is formed, and therefore the mechanism is more consistent with E1 than E2.

We then computed the kinetic isotope effect (KIE) and obtained a KIE of 2.4, in good agreement with experiment (KIE = 2.0), further corroborating the mechanism we propose.

We also computed structure **A** and **TS AB** for MOF-808 and found an activation energy of 38.2 kcal/mol, which is 3.5 kcal/mol higher than the value computed for UiO-66. The **TS AB** geometry is very similar to what we found for UiO-66, and the KIE is 2.4 (the same value as for UiO-66). According to these results, we can conclude that the TBA dehydration mechanism is the same for the two MOFs—providing further confirmation that the higher initial activity of MOF-808 is associated with the higher availability of OH groups and more rapid transport of the TBA molecules in this MOF.

DISCUSSION

Comparison of MOFs and metal oxides as catalysts. The MOFs investigated here and metal oxides such as alumina and zirconia used as catalysts for TBA dehydration are similar to each other in presenting OH groups and nearby surface Lewis acid sites (exposed Al and Zr cations, respectively). The mechanism of the TBA dehydration reaction on a mixed oxide, silica-alumina, has been inferred on the basis of experimental reaction kinetics to proceed via a carbocation intermediate, which is formed in the reaction between an acidic site with the hydroxyl group of TBA, further neutralizing a nearby basic site, with the intermediate subsequently decomposing and yielding isobutylene,[34] consistent with the mechanism shown by DFT to occur on the MOF nodes.

We emphasize the differences between the MOFs and the metal oxides: in contrast to amorphous metal oxide with their smears of heterogeneous surface sites, the MOFs offer sites in crystalline environments that can be characterized precisely for in-depth understanding of reaction mechanism guided by DFT.

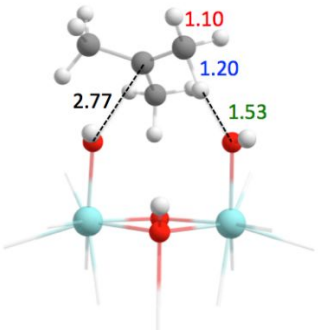

Figure 9: Transition state geometry for the *t*-butyl alcohol dehydration reaction to isobutylene and water for UiO-66 (**TS AB** in Figure 8). All linkers are omitted for clarity. Atom color code: gray for carbon, red for oxygen, white for hydrogen, light blue for zirconium. Bond length color code: black for carbon–oxygen bond, green for oxygen–hydrogen bond, blue for carbon–hydrogen bond (that is being broken), and red for another carbon–hydrogen bond (that is not participating in the reaction). All distances in Å.

Thus, an essential advantage of the MOFs is the opportunities they offer for fundamental understanding of catalysis on sites that are representative of a large class of materials—metal oxides—applied on an enormous scale in catalytic technology. But we emphasize the subtlety of the MOF catalytic sites and the need to understand their chemistry beyond the level of bulk structure and the evidence available from XRD and BET measurements. There is a need to understand the genesis of the catalytically active sites and to understand minor components in the MOFs and specifically the important role of defect sites on the MOF nodes. Understanding of the chemistry in such depth requires identification and control of these groups (in addition to linkers) that may be bonded to the nodes.

The as-synthesized MOFs incorporated formate and acetate ligands that inhibit TBA dehydration catalysis, and the catalysts had to be "broken in" by removal of these groups—by reaction with TBA to make esters, thereby forming Lewis acid sites and terminal OH groups that are responsible for the dehydration catalysis. With the benefit of DFT calculations, we see how the terminal OH groups act as catalytic sites for TBA dehydration by collaborating with neighboring Lewis acid sites. We anticipate similar mechanisms on metal oxide catalysts and posit that understanding of catalytic mechanisms on MOFs, such as that emerging from this work, will help with understanding of catalytic mechanisms metal oxides.

Comparing mechanisms of dehydration of ethanol and TBA. We have reported[13] that the active sites of UiO-66 for ethanol dehydration to diethyl ether are two adjacent defect sites, with a calculated transition state of 38.7 kcal/mol for the reaction proceeding through an S_N2 mechanism. For TBA dehydration, in contrast, the calculations show the need for only one defect, and a transition state energy of 34.7 kcal/mol for reaction proceeding through an E1 mechanism. All these results are consistent with experiment, specifically, with the TBA dehydration reaction (taking place at 150 °C) being faster than the ethanol dehydration (taking place at 200 °C).[13]

Because TBA dehydration is catalyzed by a site with both a Lewis acid site and a terminal OH group, it is highly sensitive to the density of terminal OH groups. Tuning the ligands on node defect sites by a range of post-treatment methods has been shown here to significantly influence the catalytic activity for TBA dehydration on UiO-66. In contrast, the effect of changing the ligand has been shown not to be significant for ethanol dehydration.[13] It is clear that these two alcohol dehydration reactions are valuable probes of the reactivity and catalytic properties of MOF nodes.

Acid strength and catalysis. Many results have shown that hydroxyl groups on MOF nodes are weak acids.[35-36] Our data reaffirm the conclusion, and further demonstrate that a terminal OH group on a Zr_6O_8 node is such a weak acid that it plays a role best described as that of a Brønsted base in TBA dehydration. In contrast, strong acids such as sulfonic acid resins (or *p*-toluene sulfonic acid) catalyze TBA dehydration at temperatures much lower than what we used (e.g., 70 °C), with high rates.[24]

Transport limitations. We reemphasize the importance of being aware of possible transport limitations in MOF catalysis. MOF pores are comparable to those in zeolites, which not only provide confined environment for reactions, but also limit the transport of reactions. Transport limitations have been reported for MOF-catalyzed reactions, for example, for reactions catalyzed by MOF-encapsulated palladium or platinum nanoparticles.[37-38] The reported results show that reaction rates decreased markedly as reactant size increased. However, all these results, like those determined in our work, are qualitative, falling short of determining quantitative measures of the transport rates and intrinsic catalytic reaction rates.

Our results indicate that the reactions between TBA and formate and acetate ligands on the nodes to form esters are strongly limited by the small pore size of UiO-66 (the data are consistent with the inference that the esters are too large to be transported readily through the pores of UiO-66—and this transport limitation minimizes the catalytic activity of UiO-66. However, after removal of the formate and acetate ligands (either by reaction with methanol or by high-temperature dehydration), the number of accessible active sites (defects with terminal OH groups) increases markedly as they become accessible to TBA for dehydration to form isobutylene. We infer that the pore aperture diameter should be regarded as larger than the nominal (crystallographically determined) value of 6 Å for the ideal MOF, because of the missing linkers and nodes; consequently, the limitations of transport of TBA and isobutylene in the pores of UiO-66 are less than would be expected on just the basis of the crystallographic data for the ideal MOF. There is much to learn yet about transport/reaction tradeoffs in MOF catalysis.

Stabilities. We further emphasize the importance of being aware of potential MOF stability limitations in investigations of MOF catalysis, both because MOF stabilities are important criteria for potential application and because MOF stabilities may depend in complex ways on their environments. MOF stabilities are potentially influenced by numbers of node-linker bonds, node-linker bond strengths, mechanisms of node-linker bond breaking, properties of node center elements, etc.[39] Our data provide evidence showing that the number of defects is also crucial for the stabilities of our MOFs. MOF-808, among those known that incorporate Zr_6O_8 nodes, is the one with the greatest number of node vacancies. This might at first be considered an advantage, implying high catalytic activity, but it is also a major disadvantage, implying a low stability compared with UiO-66, which has a much lower number of defect sites per node, at least under our alcohol dehydration conditions. One should be aware of potential tradeoffs related to reactivity and stability of MOFs.

CONCLUSIONS

Terminal OH groups on defect sites of Zr_6O_8 nodes of MOF-808 and UiO-66 catalyze the dehydration of TBA, with the rates depending on ligands on defect sites and intrapore transport limitations. Because of their well-defined structures, the MOF nodes are excellent platforms for fundamental understanding of catalytic sites and reaction mechanisms related to those on metal oxides. MOF-808 and UiO-66, which have approximately 6 and 1 vacancies per Zr_6O_8 node, respectively, were compared with alumina and zirconia as catalysts for TBA dehydration. The greater number of vacancies on MOF-808 nodes accounts for its initially higher activity than that of UiO-66—but these vacancies also limit the stability of this MOF as a catalyst. DFT calculations show that the OH groups on UiO-66 and MOF-808 act as Brønsted basic sites, and they are generated by the removal of formate/acetate ligands initially present on the nodes via esterification reactions with the alcohol. The calculations indicate an E1 elimination reaction, with an activation barrier for TBA dehydration on UiO-66 that is 4 kcal/mol lower than that reported for ethanol dehydration on the same MOF, consistent with higher observed reactivity of TBA. The computational results further suggest that the binding of two TBA molecules to node Zr atoms during the esterification reaction helps in lowering the total activation energy of this reaction.

EXPERIMENTAL AND COMPUTATIONAL METHODS

Synthesis of UiO-66 with acetic acid modulator. $ZrCl_4$ (0.080 g, 0.343 mmol) and 0.7 mL of acetic acid (modulator) were dissolved in 20 mL of DMF in a 8-dram vial by using ultrasound for 5 min. The linker precursor benzene-1,4-dicarboxylic acid (H_2BDC, 0.057 g, 0.343 mmol) was then added into the solution and dissolved by ultrasound for about 5 min. The vials were kept in an oven at 120 °C under static conditions for 24 h. White precipitates were produced, and they were isolated by centrifugation after cooling to room temperature. The solids were washed with DMF three times to remove unreacted precursors and with acetone six times to remove DMF. Then the powder was dried at room temperature and activated at 120 °C for 12 h under high vacuum.

Synthesis of MOF-808 with formic acid as modulator. $ZrOCl_2 \cdot 8H_2O$ (0.253 g, 0.785 mmol) and 10 mL of formic acid (88 wt% in water, 0.156 mol) were dissolved in 10 mL of DMF in an 8 dram vial by using ultrasound for 10 min. The linker precursor benzene-1,3,5-tricarboxylic acid (H_3BTC, 55 mg, 0.262 mmol) was then added into the solution and dissolved by ultrasound for about 10 min. The vials were kept in an oven at 120 °C under static conditions for 48 h. White precipitates were produced, and they were isolated by centrifugation after cooling to room temperature. The solids were washed with DMF three times to remove unreacted precursors and with acetone six times to remove DMF. Then the powder was dried at room temperature and activated at 120 °C for 12 h under high vacuum.

Post-treatment of UiO-66 with methanol vapor. Post-treatment of UiO-66 with methanol vapor was carried out in a conventional laboratory once-through tubular plug-flow reactor at 200 °C and 1 bar for 48 h. The MOF sample (200 mg) was loaded into the reactor in an argon-filled glovebox. Methanol was carried into the reactor in a stream of helium carrier gas that flowed through a methanol-filled bubbler with the temperature controlled at 25 °C. The sample is designated as UiO-66-OCH_3.

Post-treatment of UiO-66 with water vapor. The UiO-66-OCH_3 sample was further treated with water vapor in the flow reactor at 150 °C and 1 bar for 10 h. The MOF sample (200 mg) was loaded into the reactor in an argon-filled glovebox. Water was carried into the reactor in a stream of helium carrier gas that flowed through a water-filled bubbler with temperature controlled at 25 °C. The sample is designated as UiO-66-OH.

Post-treatment of UiO-66 at 320 °C. UiO-66 was dehydrated at 320 °C under high vacuum for 12 h. The sample is designated as UiO-66-320.

Infrared spectroscopy. A Bruker IFS 66v/S spectrometer with a spectral resolution of 2 cm^{-1} was used to collect transmission IR spectra of powder samples. Approximately 30 mg of solid sample in an argon-filled glove box was pressed into a thin wafer and loaded into a cell that served a flow reactor (In-situ Research Institute, Inc., South Bend, IN). The cell was sealed and connected to a flow system that allowed recording of spectra while the reactant gases flowed through the cell at reaction temperature. Each spectrum is the average of 64 scans.

BET surface area measurements. All N_2 isotherms were measured with a Micromeritics 3Flex Surface Characterization Analyzer instrument. Measurements were performed at -196 °C, with the temperature held constant with a liquid nitrogen bath. Consistency criteria were adapted to choose an appropriate pressure range for BET surface area calculations.

^{1}H NMR spectroscopy. Samples were prepared by weighing 10 mg of MOF into a 1.5 ml vial. A 600 µL portion of the digestion medium was then added to the tube. The digestion medium was 1-*M* NaOH in D_2O. The vials were capped and inverted 2–3 times before allowing the samples to digest over a period of 24 h. This OH-based procedure dissolves only the organic portion of the MOF (linker, modulator, solvent, etc.), while the inorganic component drops out as ZrO_2. After 24 h, the clear supernatant solution was transferred to an NMR tube. Liquid ^{1}H NMR spectra were recorded with a Bruker Avance DPX-500 NMR Spectrometer (500 MHz). The relaxation delay (d1) was set to 20 s to ensure that reliable integrals were obtained, allowing for the accurate determination of the relative concentrations of the molecular components. The number of scans was 32.

Powder X-ray Diffraction (PXRD). PXRD patterns were obtained using a Panlytical X-ray Diffractometer Model X'Pert Pro MRD. Measurements were made over a range of $2° < 2\theta < 20°$ in 0.05 step size at a scanning rate of 1 deg/min.

Catalytic Reaction Experiments. TBA dehydration catalysis was carried out in a conventional laboratory once-through tubular plug-flow reactor at °C and 1 bar. Particles of the MOF catalyst (25–100 mg) were mixed with 2 g of particles of inert, nonporous α-Al_2O_3 and loaded into the reactor in an argon-filled glove box. The feed partial pressures were 75 mbar of TBA and

925 mbar of helium, with a total flow rate of 5.4 mL(NTP)/min (TBA was carried into the reactor with helium flowing through a bubbler, and all of the gas lines downstream of the bubbler were held at 120 °C to avoid condensation of the TBA and reaction products). Products were analyzed with an on-line Agilent 6890 gas chromatograph. The conversions to isobutylene were typically < 10%, and the reactor was well approximated as differential.

Computational methods. DFT geometry optimizations and frequency calculations were performed using the M06-L local density functional[40] and the Gaussian 09[41] software package. The def2-SVP basis set was employed for H, C, and O atoms, and the def2-TZVPP basis set[42-43] was employed for the Zr atoms. Only for the TBA dehydration reaction, in order to compare the results with a previous study on ethanol dehydration, same computational details as previously reported[13] were used (see SI, section S2.5). The SDD pseudopotential[44] was employed to describe the core electrons in Zr. An ultrafine grid was used for performing numerical integrations. The nature of the stationary points (minima or transition states) along the potential energy surfaces was verified through the computation of vibrational frequencies, which were also employed to calculate enthalpic and entropic contributions at 150 °C. The frequencies below 50 cm^{-1} were replaced by 50 cm^{-1} when computing all the free energies reported in this work. Computational details for periodic boundary condition calculations are reported in Section S2.6 of the SI.

ASSOCIATED CONTENT

Supporting Information. Experimental and computational details are reported, primarily IR spectra, catalytic activities, ^{1}H NMR spectra, desorption curves, SEM images and Cartesian coordinates with its associated energies. This material is available free of charge via the Internet at http://pubs.acs.org.

AUTHOR INFORMATION

Corresponding Authors

***bcgates@ucdavis.edu (B.C.G.)**
***gagliard@umn.edu (L.G.)**

Notes

The authors declare no competing financial interest.

Author Contributions

† These authors contributed equally to this work

ACKNOWLEDGMENTS

This work was supported as part of the Inorganometallic Catalyst Design Center, an Energy Frontier Research Center funded by the U.S. Department of Energy (DOE), Office of Science, Basic Energy Sciences (DE-SC0012702). We thank Dr. Ping Yu of the NMR facility at the University of California, Davis, for help with the ^{1}H NMR measurements.

ORCID

Dong Yang: 0000-0002-3109-0964
Carlo Alberto Gaggioli: 0000-0001-9105-8731
Melike Babucci: 0000-0001-7785-3755
Laura Gagliardi: 0000-0001-5227-1396
Bruce C. Gates: 0000-0003-0274-4882

REFERENCES

(1) Ferey, G., Hybrid Porous Solids: Past, Present, Future. *Chem. Soc. Rev.* **2008,** *37*, 191-214.
(2) Horike, S.; Shimomura, S.; Kitagawa, S., Soft Porous Crystals. *Nat. Chem.* **2009,** *1*, 695-704.
(3) Furukawa, H.; Cordova, K. E.; O'Keeffe, M.; Yaghi, O. M., The Chemistry and Applications of Metal-Organic Frameworks. *Science* **2013,** *341*, 1230444.
(4) Jiang, J. C.; Yaghi, O. M., Bronsted Acidity in Metal-Organic Frameworks. *Chem. Rev.* **2015,** *115*, 6966-6997.
(5) Dhakshinamoorthy, A.; Li, Z.; Garcia, H., Catalysis and Photocatalysis by Metal Organic Frameworks. *Chem. Soc. Rev.* **2018,** *47*, 8134-8172.
(6) Pascanu, V.; Miera, G. G.; Inge, A. K.; Martin-Matute, B., Metal-Organic Frameworks as Catalysts for Organic Synthesis: A Critical Perspective. *J. Am. Chem. Soc.* **2019,** *141*, 7223-7234.
(7) Yang, D.; Gates, B. C., Catalysis by Metal Organic Frameworks: Perspective and Suggestions for Future Research. *ACS Catal.* **2019,** *9*, 1779-1798.
(8) Wang, Q.; Astruc, D., State of the Art and Prospects in Metal–Organic Framework (MOF)-Based and MOF-Derived Nanocatalysis. *Chem. Rev.* **2020,** *120*, 1438-1511.
(9) Cavka, J. H.; Jakobsen, S.; Olsbye, U.; Guillou, N.; Lamberti, C.; Bordiga, S.; Lillerud, K. P., A New Zirconium Inorganic Building Brick Forming Metal Organic Frameworks with Exceptional Stability. *J. Am. Chem. Soc.* **2008,** *130*, 13850-13851.
(10) Mondloch, J. E.; Bury, W.; Fairen-Jimenez, D.; Kwon, S.; DeMarco, E. J.; Weston, M. H.; Sarjeant, A. A.; Nguyen, S. T.; Stair, P. C.; Snurr, R. Q.; Farha, O. K.; Hupp, J. T., Vapor-Phase Metalation by Atomic Layer Deposition in a Metal-Organic Framework. *J. Am. Chem. Soc.* **2013,** *135*, 10294–10297.
(11) Vermoortele, F.; Bueken, B.; Le Bars, G.; Van de Voorde, B.; Vandichel, M.; Houthoofd, K.; Vimont, A.; Daturi, M.; Waroquier, M.; Van Speybroeck, V.; Kirschhock, C.; De Vos, D. E., Synthesis Modulation as a Tool To Increase the Catalytic Activity of Metal-Organic Frameworks: The Unique Case of UiO-66(Zr). *J. Am. Chem. Soc.* **2013,** *135*, 11465-11468.
(12) Shearer, G. C.; Chavan, S.; Bordiga, S.; Svelle, S.; Olsbye, U.; Lillerud, K. P., Defect Engineering: Tuning the Porosity and Composition of the Metal-Organic Framework UiO-66 via Modulated Synthesis. *Chem. Mater.* **2016,** *28*, 3749-3761.
(13) Yang, D.; Ortuño, M. A.; Bernales, V.; Cramer, C. J.; Gagliardi, L.; Gates, B. C., Structure and Dynamics of Zr_6O_8 Metal-Organic Framework Node Surfaces Probed with Ethanol Dehydration as a Catalytic Test Reaction. *J. Am. Chem. Soc.* **2018,** *140*, 3751-3759.
(14) Wei, R.; Gaggioli, C. A.; Li, G.; Islamoglu, T.; Zhang, Z.; Yu, P.; Farha, O. K.; Cramer, C. J.; Gagliardi, L.; Yang, D.; Gates, B. C., Tuning the Properties of Zr_6O_8 Nodes in the Metal Organic Framework UiO-66 by Selection of Node-Bound Ligands and Linkers. *Chem. Mater.* **2019,** *31*, 1655-1663.
(15) Wu, H.; Chua, Y. S.; Krungleviciute, V.; Tyagi, M.; Chen, P.; Yildirim, T.; Zhou, W., Unusual and Highly Tunable

Missing-Linker Defects in Zirconium Metal-Organic Framework UiO-66 and Their Important Effects on Gas Adsorption. *J. Am. Chem. Soc.* **2013,** *135*, 10525-10532.
(16) Jiang, J. C.; Gandara, F.; Zhang, Y. B.; Na, K.; Yaghi, O. M.; Klemperer, W. G., Superacidity in Sulfated Metal-Organic Framework-808. *J. Am. Chem. Soc.* **2014,** *136*, 12844-12847.
(17) Trickett, C. A.; Popp, T. M. O.; Su, J.; Yan, C.; Weisberg, J.; Huq, A.; Urban, P.; Jiang, J.; Kalmutzki, M. J.; Liu, Q.; Baek, J.; Head-Gordon, M. P.; Somorjai, G. A.; Reimer, J. A.; Yaghi, O. M., Identification of the Strong Brønsted Acid Site in a Metal–Organic Framework Solid Acid Catalyst. *Nat. Chem.* **2019,** *11*, 170–176,
(18) Yang, D.; Bernales, V.; Islamoglu, T.; Farha, O. K.; Hupp, J. T.; Cramer, C. J.; Gagliardi, L.; Gates, B. C., Tuning the Surface Chemistry of Metal Organic Framework Nodes: Proton Topology of the Metal-Oxide-Like Zr_6 Nodes of UiO-66 and NU-1000. *J. Am. Chem. Soc.* **2016,** *138*, 15189-15196.
(19) Caratelli, C.; Hajek, J.; Cirujano, F. G.; Waroquier, M.; Xamena, F. X. L. I.; Van Speybroeck, V., Nature of Active Sites on UiO-66 and Beneficial Influence of Water in the Catalysis of Fischer Esterification. *J. Catal.* **2017,** *352*, 401-414.
(20) Mondloch, J. E.; Katz, M. J.; Isley, W. C.; Ghosh, P.; Liao, P. L.; Bury, W.; Wagner, G.; Hall, M. G.; DeCoste, J. B.; Peterson, G. W.; Snurr, R. Q.; Cramer, C. J.; Hupp, J. T.; Farha, O. K., Destruction of Chemical Warfare Agents Using Metal-Organic Frameworks. *Nat. Mater.* **2015,** *14*, 512-516.
(21) Hoffman, A. E. J.; Vanduyfhuys, L.; Nevjestic, I.; Wieme, J.; Rogge, S. M. J.; Depauw, H.; Van der Voort, P.; Vrielinck, H.; Van Speybroeck, V., Elucidating the Vibrational Fingerprint of the Flexible Metal-Organic Framework MIL-53(Al) Using a Combined Experimental/Computational Approach. *J. Phys. Chem. C* **2018,** *122*, 2734-2746.
(22) Benzaqui, M.; Pillai, R. S.; Sabetghadam, A.; Benoit, V.; Normand, P.; Marrot, J.; Menguy, N.; Montero, D.; Shepard, W.; Tissot, A.; Martineau-Corcos, C.; Sicard, C.; Mihaylov, M.; Carn, F.; Beurroies, I.; Llewellyn, P. L.; De Weireld, G.; Hadjiivanov, K.; Gascon, J.; Kapteijn, F.; Maurin, G.; Steunou, N.; Serre, C., Revisiting the Aluminum Trimesate-Based MOF (MIL-96): From Structure Determination to the Processing of Mixed Matrix Membranes for CO_2 Capture. *Chem. Mater.* **2017,** *29*, 10326-10338.
(23) Volkringer, C.; Leclerc, H.; Lavalley, J.-C.; Loiseau, T.; Ferey, G.; Daturi, M.; Vimont, A., Infrared Spectroscopy Investigation of the Acid Sites in the Metal-Organic Framework Aluminum Trimesate MIL-100(Al). *J. Phys. Chem. C* **2012,** *116*, 5710-5719.
(24) Gates, B.C.; Wisnouskas, J. S.; Heath, H. W., Jr. The Dehydration of *t*-Butyl Alcohol Catalyzed by Sulfonic Acid Resin. *J. Catal.* **1972,** *24*, 320-327.
(25) Frilette, V. J.; Mower, E. B.; Rubin, M. K., Kinetics of Dehydration of tert-Butyl Alcohol Catalyzed by Ion Exchange Resins. *J. Catal.* **1964,** *3*, 25-31.
(26) Furukawa, H.; Gandara, F.; Zhang, Y. B.; Jiang, J. C.; Queen, W. L.; Hudson, M. R.; Yaghi, O. M., Water Adsorption in Porous Metal-Organic Frameworks and Related Materials. *J. Am. Chem. Soc.* **2014,** *136*, 4369-4381.
(27) Stepanian, S. G.; Reva, I. D.; Radchenko, E. D.; Sheina, G. G., Infrared Spectra of Benzoic Acid Monomers and Dimers in Argon Matrix. *Vib. Spectrosc.* **1996,** *11*, 123-133.
(28) Chen, X.; Lyu, Y. H.; Wang, Z. Y.; Qiao, X.; Gates, B. C.; Yang, D., Tuning $Zr_{12}O_{22}$ Node Defects as Catalytic Sites in the Metal–Organic Framework **hcp** UiO-66. *ACS Catal.* **2020,** *10*, 2906-2914.
(29) Shi, B. C.; Dabbagh, H. A.; Davis, B. H., Catalytic Dehydration of Alcohols. Kinetic Isotope Effect for the Dehydration of *t*-Butanol. *Top. Catal.* **2002,** *18*, 259-264.
(30) Jai, J. R.; Pillai, C. N., Catalytic Dehydration of Alcohols over Alumina: Mechanism of Ether Formation. *J. Catal.* **1964,** *9*, 322-330.
(31) Kipkemboi, P. K.; Kiprono, P. C.; Sanga, J. J., Vibrational Spectra of *t*-Butyl Alcohol, *t*-Butylamine and *t*-Butyl Alcohol plus *t*-Butylamine Binary Liquid Mixtures. *B. Chem. Soc. Ethiopia* **2003,** *17*, 211-218.
(32) Lynch, K, C. T.; Mazdiyasni, S.; Smith, J. S.; Crawford, W. J., Infrared Spectra of Transition Metal Alkoxides. *Anal. Chem.* **1964,** *36*, 2332-2337.
(33) Kiss, I.; Jákli, G.; Jancsó, G.; Illy, H., Vapor Pressures of Some Deuterated Alcohols and Amines. *J. Chem. Phys.* **1967,** *47*, 4851-4852.
(34) Figueras, F.; Nohl, A.; Mourgueas, L. D.; Trambouze, Y., Dehydration of Methanol and *tert*-Butyl Alcohol on Silica-Alumina. *T. Faraday Soc.* **1971,** *67*, 1155-1163.
(35) Driscoll, D. M.; Troya, D.; Usov, P. M.; Maynes, A. J.; Morris, A. J.; Morris, J. R., Characterization of Undercoordinated Zr Defect Sites in UiO-66 with Vibrational Spectroscopy of Adsorbed CO. *J. Phys. Chem. C* **2018,** *122*, 14582-14589.
(36) Volkringer, C.; Leclerc, H.; Lavalley, J. C.; Loiseau, T.; Ferey, G.; Daturi, M.; Vimont, A., Infrared Spectroscopy Investigation of the Acid Sites in the Metal-Organic Framework Aluminum Trimesate MIL-100(Al). *J. Phys. Chem. C* **2012,** *116*, 5710-5719.
(37) Wang, B. Q.; Liu, W. X.; Zhang, W. N.; Liu, J. F., Nanoparticles@nanoscale Metal-Organic Framework Composites as Highly Efficient Heterogeneous Catalysts for Size- and Shape-Selective Reactions. *Nano Res.* **2017,** *10*, 3826-3835.
(38) Zhang, W. N.; Lu, G.; Cui, C. L.; Liu, Y. Y.; Li, S. Z.; Yan, W. J.; Xing, C.; Chi, Y. R.; Yang, Y. H.; Huo, F. W., A Family of Metal-Organic Frameworks Exhibiting Size-Selective Catalysis with Encapsulated Noble-Metal Nanoparticles. *Adv. Mater.* **2014,** *26*, 4056-4060.
(39) Burtch, N. C.; Jasuja, H.; Walton, K. S., Water Stability and Adsorption in Metal-Organic Frameworks. *Chem. Rev.* **2014,** *114*, 10575-10612.
(40) Zhao, Y.; Truhlar, D. G., A New Local Density Functional for Main-Group Thermochemistry, Transition Metal Bonding, Thermochemical Kinetics, and Noncovalent Interactions. *J. Chem. Phys.* **2006,** *125*, 194101.
(41) Frisch, M. J.; Trucks, G. W.; Schlegel, H. B.; Scuseria, G. E.; Robb, M. A.; Cheeseman, J. R.; Scalmani, G.; Barone, V.; Mennucci, B.; Petersson, G. A.; Nakatsuji, H.; Caricato, M.; Li, X.; Hratchian, H. P.; Izmaylov, A. F.; Bloino, J.; Zheng, G.; Sonnenberg, J. L.; Hada, M.; Ehara, M.; Toyota, K.; Fukuda, R.; Hasegawa, J.; Ishida, M.; Nakajima, T.; Honda, Y.; Kitao, O.; Nakai, H.; Vreven, T.; Montgomery, J. J. A.; Peralta, J. E.; Ogliaro, F.; Bearpark, M.; Heyd, J. J.; Brothers, E.; Kudin, K. N.; Staroverov, V. N.; Kobayashi, R.; Normand, J.; Raghavachari, K.; Rendell, A.; Burant, J. C.; Iyengar, S. S.; Tomasi, J.; Cossi, M.; Rega, N.; Millam, J. M.; Klene, M.; Knox, J. E.; Cross, J. B.; Bakken, V.; Adamo, C.; Jaramillo, J.; Gomperts, R.; Stratmann, R. E.; Yazyev, O.; Austin, A. J.;

Cammi, R.; Pomelli, C.; Ochterski, J. W.; Martin, R. L.; Morokuma, K.; Zakrzewski, V. G.; Voth, G. A.; Salvador, P.; Dannenberg, J. J.; Dapprich, S.; Daniels, A. D.; Farkas, Ö.; Foresman, J. B.; Ortiz, J. V.; Cioslowski, J.; Fox, D. J. Gaussian 09, Revision E.01; Gaussian, Inc.: Wallingford, CT, 2009.
(42) Weigend, F., Accurate Coulomb-Fitting Basis Sets for H to Rn. *Phys. Chem. Chem. Phys.* **2006,** *8*, 1057-1065.
(43) Weigend, F.; Ahlrichs, R., Balanced Basis Sets of Split Valence, Triple Zeta Valence and Quadruple Zeta Valence Quality for H to Rn: Design and Assessment of Accuracy. *Phys. Chem. Chem. Phys.* **2005,** *7*, 3297-3305.
(44) Hay, P. J.; Dunning Jr, T. H., Modern Theoretical Chemistry, Methods of Electronic Structure Theory. **1976,** *3*.

TOC